

1 Revision 1

2 **Inherited Eocene magmatic tourmaline captured by the Miocene Himalayan**
3 **leucogranites**

4 **Jinsheng Han^a, Pete Hollings^b, Fred Jourdan^c, Yunchuan Zeng^d, Huayong Chen^{a,*}**

5 *a. Key Laboratory of Mineralogy and Metallogeny, Guangzhou Institute of*
6 *Geochemistry, Chinese Academy of Sciences, Guangzhou 510640, China*

7 *b. Department of Geology, Lakehead University, 955 Oliver Road, Thunder Bay,*
8 *Ontario P7B 5E1, Canada*

9 *c. Western Australian Argon Isotope Facility, Department of Applied Geology and*
10 *JdL-CMS, Curtin University, GPO Box U1987, Perth, WA 6845, Australia*

11 *d. State Key Laboratory of Geological Processes and Mineral Resources, School of*
12 *Earth Science and Resources, China University of Geosciences, Beijing 100083,*
13 *China*

14 *Corresponding Author: Huayong Chen

15 Key Laboratory of Mineralogy and Metallogeny, Guangzhou Institute of
16 Geochemistry, Chinese Academy of Sciences, Guangzhou 510640, China

17 Tel: +86-13926101976; Email: huayongchen@gig.ac.cn

18 **Abstract**

19 The Miocene Cuonadong leucogranites, in the easternmost section of the Tethyan
20 Himalaya, Southern Tibet are characterized by two types of tourmaline. Tourmaline
21 occurs as needle-like crystals in the two-mica \pm tourmaline granites (Tur G) and large
22 patches in the pegmatites (Tur P). Both the granite and the pegmatites yield Miocene

23 ages (ca. 20 Ma) based on monazite U(-Th)-Pb dating, whereas $^{40}\text{Ar}/^{39}\text{Ar}$
24 geochronology of the coarse-grained tourmalines (Tur P) crosscut by pegmatite veins
25 yielded an Eocene mini-plateau age of 43 ± 6 Ma. Major element concentrations of
26 tourmaline indicate that both Tur P and Tur G belong to the schorl group with a
27 magmatic origin, but trace elements such as V indicate that they are not cogenetic.
28 Boron isotopes suggest that Tur P (average -9.76%) was derived from typical crustal
29 sources whereas Tur G (average -7.65%) contains relatively more mafic input. The
30 capture of Eocene tourmaline by the Miocene leucogranites at Cuonadong suggests
31 that the crustally-derived Eocene magmatism may have occurred in the southern
32 Tethyan Himalaya. Identification of the inherited magmatic tourmaline (Tur P),
33 although not common, challenges the current application of tourmaline chemistry to
34 the investigation of magmatic-hydrothermal systems.

35 **Keywords:** Inherited tourmaline, Himalayan leucogranite, $^{40}\text{Ar}/^{39}\text{Ar}$ and U(-Th)-Pb
36 geochronology, B isotope

37 **Introduction**

38 The Himalayan continent-continent collisional belt resulted from the
39 convergence and collision of India and Asia along the Indus-Tsangpo Suture zone that
40 began in the Cenozoic (Yin and Harrison, 2000). Crustal anatexis related to this
41 large-scale continental collision resulted in the formation of a series of leucogranites
42 (Yin et al., 2006), which generally consist of cogenetic two-mica-, tourmaline- and
43 garnet-bearing rocks, with widespread dikes and stocks of pegmatite (Wu et al., 2020).
44 Two sub-parallel E-trending leucogranite belts, the Higher Himalayan and Tethyan

45 Himalayan ([Supplementary Figs. 1a, b](#)), have been recognized, with the former
46 exposed along the South Tibetan Detachment System (STDS) in the Higher
47 Himalayan Sequence (HHS) and the latter mainly occurring in the core of the North
48 Himalayan Gneiss Domes (NHGDS) ([Supplementary Fig. 1b; Wu et al., 2020](#)). The
49 majority of the leucogranites have yielded Miocene ages (26–7 Ma), with a small
50 number of samples with Eocene ages (46–30 Ma) being found in the eastern most
51 region of the Tethyan Himalayan ([Wu et al., 2020](#)). The Miocene and Eocene
52 leucogranites were proposed to have formed from distinct episodes of crustal anatexis
53 with clearly separated distribution in Southern Tibet ([Supplementary Fig. 1; Patiño](#)
54 [Douce and Harris, 1998; Hou et al., 2012](#)). Tourmaline, which is very common in the
55 Himalayan leucogranites and typically the dominant reservoir of B in the rocks, is
56 stable in various P-T-X conditions and could record the physical and chemical
57 conditions under which it formed ([Marschall and Jiang, 2011; Slack and Trumbull,](#)
58 [2011](#)). Due to its robustness, tourmaline chemistry has recently been used to
59 investigate the genesis of Himalayan leucogranites ([Yang et al., 2015; Hu et al., 2018](#)).
60 However, these studies relied on the assumption that the tourmalines formed
61 cogenetically with their magmatic host rocks as is widely interpreted in most of the
62 global tourmaline occurrences ([van Hinsberg et al., 2011](#)). Following the approach
63 illustrated by [Thern et al. \(2020\)](#), we applied the $^{40}\text{Ar}/^{39}\text{Ar}$ dating method to
64 coarse-grained tourmalines from the Miocene Cuonadong leucogranite, which yielded
65 Eocene ages. The identification of inherited tourmalines not only contributes new
66 insights into the Himalayan collisional orogeny, but also provides constraints on

67 application of tourmaline chemistry to petrological studies.

68 **Cuonadong tourmaline petrography**

69 The Cuonadong leucogranite is located in the easternmost section of the Tethyan
70 Himalaya ([Supplementary Fig. 1a](#)) and consists mainly of two-mica ± tourmaline
71 granite and granitic pegmatite. The pegmatites commonly occur as veins or pockets in
72 the leucogranites, without clear boundaries between them ([Supplementary Fig. 2](#)).
73 The wall rocks consist mainly of sandstone, mudstone, slate and schist intercalated
74 with carbonates ([Li et al., 2017](#); [Zhou et al., 2019](#)). Two types of tourmalines have
75 been identified in the Cuonadong leucogranites, large tourmaline crystals in the
76 pegmatites (Tur P; [Figs. 1a-d](#)) and needle-like tourmaline crystals in the two-mica ±
77 tourmaline granite (Tur G; [Fig. 1e](#)). The Tur P are pervasively distributed in the
78 pegmatites, and are cut by abundant quartz/pegmatite/quartz-muscovite veins along
79 fractures ([Figs. 1a-d](#); [Supplementary Fig. 3a](#)). Abundant micro-fractures and some
80 zircon inclusions were observed in the Tur P in backscattered electron (BSE) images
81 ([Supplementary Fig. 3b](#)). The Tur G occur as disseminated needle-like crystals,
82 coexisting with muscovite, quartz and feldspar in the granites and show clear core-rim
83 zoning in thin section but not in BSE images ([Fig. 1e](#), [Supplementary Figs. 2c-d](#)).
84 Both Tur P and Tur G are commonly homogeneous in BSE images.

85 **Methods**

86 Tourmaline $^{40}\text{Ar}/^{39}\text{Ar}$ analyses were performed on one pegmatite sample using
87 an ARGUS VI at the Western Australian Argon Isotope Facility, Curtin University.
88 Monazite LA ICP-MS U(-Th)-Pb geochronology of both granite and pegmatite were

89 performed utilizing a system consisting of ASI RESOLution S-155 193nm ArF
90 Excimer laser coupled to Thermo Scientific iCAP Qc quadrupole ICP-MS at the State
91 Key Laboratory for Mineral Deposits Research, Nanjing University, China. The
92 detailed analytical procedures and conditions of all the above and other methods are
93 listed in [Supplementary Appendix A](#).

94 **Results**

95 The Tur P in the pegmatites yielded a $^{40}\text{Ar}/^{39}\text{Ar}$ mini-plateau age of 43 ± 6 Ma
96 (MSWD = 0.8; P = 0.57; [Supplementary Table 1](#); [Fig. 2a](#)), which includes 66.3% of
97 the total amount of ^{39}Ar that was released. Commonly for low potassium minerals
98 containing excess argon, a saddle-shaped ^{39}Ar release spectrum during stepped
99 heating will be displayed ([Kelley, 2002](#)), which is not shown in our Tur P data
100 indicating the absence of excess ^{40}Ar in the lattice during crystallization ([Qiu et al.,](#)
101 [2007](#)), suggesting that the calculated Ar plateau age represents the true age of
102 tourmaline, rather than the result of excess argon. The high apparent step ages (older
103 than 70 Ma) displayed within the first few percent of gas released are likely attributed
104 to excess ^{40}Ar in fluid inclusions or the margins of the crystals. We calculated a
105 mini-inverse isochron age of 58 ± 15 Ma (MSWD = 0.8; P = 0.63), associated with a
106 trap $^{40}\text{Ar}/^{36}\text{Ar}$ ratio of 251 ± 52 . This ratio, although imprecise, does overlap with
107 atmospheric compositions (~ 298.6 ; [Lee et al., 2006](#)) which would indicate the
108 mini-plateau age (which assumes a $^{40}\text{Ar}/^{36}\text{Ar}$ ratio of 298.6) is correct. Note that a
109 sub-atmospheric ratio and the absence of saddle-shaped ^{39}Ar release spectrum suggest
110 that no excess ^{40}Ar is present in this part of the age spectrum. In addition, some

111 monazite grains in the granite yielded similar ages to the mini-plateau age (Fig. 2b).
112 In general, the mini-plateau and mini-inverse isochron ages of 43 ± 6 Ma and 58 ± 15
113 Ma (Fig. 2a), respectively, overlap with each other and are both clearly older than the
114 U-Th-Pb age of ca. 20 Ma for the monazite (Figs. 2b and 2c).

115 Monazite often has excess ^{206}Pb , resulting in high $^{206}\text{Pb}/^{238}\text{U}$ age and reverse
116 discordance on U-Pb diagrams (Schärer, 1984). Thus, the $^{207}\text{Pb}/^{235}\text{U}$ may provide the
117 best estimate of the age. However, the Himalaya leucogranites are too young to yield
118 reliable $^{207}\text{Pb}/^{235}\text{U}$ (Wu et al., 2015). As a result, the Th-Pb ages are often used for
119 monazite geochronology of the Himalaya leucogranites (Harrison et al., 1995).
120 Monazite grains from the two-mica \pm tourmaline granite sample yielded a $^{208}\text{Pb}/^{232}\text{Th}$
121 age of 20.3 ± 0.2 Ma, with two grains having older ages of 45.2 ± 1.6 Ma and $43.9 \pm$
122 1.4 Ma (Supplementary Table 2; Fig. 2b). The older ages are consistent with the
123 plateau $^{40}\text{Ar}/^{39}\text{Ar}$ age of the Tur P and represent inherited monazite crystals. The
124 pegmatite sample yielded a monazite $^{208}\text{Pb}/^{232}\text{Th}$ age of 20.5 ± 0.1 Ma
125 (Supplementary Table 2; Fig. 2c), nearly identical to the two-mica granite ages and
126 distinct from the plateau $^{40}\text{Ar}/^{39}\text{Ar}$ age of Tur P.

127 Major and trace element compositions of the tourmaline are provided in
128 Supplementary Table 3. Both Tur P and Tur G are dominantly schorl end-member
129 tourmalines, with Fe/(Fe+Mg) ratios of 0.67–0.85 for Tur P, 0.75–0.87 for the Tur G
130 cores and 0.74–0.87 the Tur G rims. Tourmaline grains have wide ranges of Ti
131 (0.04–0.15 apfu for the Tur P, 0.01–0.09 apfu for the Tur G core, 0.02–0.11 apfu for
132 the Tur G rim) and Al concentrations (6.23–6.55 apfu for the Tur P, 6.04–6.50 apfu for

133 the Tur G core and 6.00–6.70 apfu for the Tur G rim). On the Al-Fe-Mg diagram, both
134 the Tur P and the Tur G plot in the field of Li-poor granitoids and associated
135 pegmatites and aplites, suggesting a magmatic origin (Supplementary Fig. 4). The
136 trace element compositions in tourmaline are commonly low, from tens of ppm for the
137 LILE (Large Ion Lithophile Elements) to ppb for the HFSE (High Field Strength
138 Elements). The concentrations of Cr, Co, Ni, Sr, V and Sc in Tur P are commonly
139 higher than those of the Tur G. The Tur P have a wider range and lower average
140 $\delta^{11}\text{B}$ values than the Tur G, with the former ranging from -14.14‰ to -7.06‰
141 (average -9.76‰) and the latter from -8.82‰ to -6.79‰ (average -7.69‰, Tur G core)
142 and -10.25‰ to -5.83‰ (average -7.61‰, Tur G rim; Fig. 2d), respectively. The
143 $\delta^{11}\text{B}$ values for Tur P and Tur G are well within the range reported for other granites
144 in the world (Supplementary Table 4; ca. -15‰ and ca. -5‰, Marschall and Jiang,
145 2011).

146 Discussion and implications

147 Tourmaline is common in highly evolved granites and pegmatites and has been
148 widely studied to investigate their petrogenesis (e.g., Yang et al., 2015) and to
149 decipher the process of fluid flow during the magmatic-hydrothermal transition
150 (Launay et al., 2018). All of these studies depend on the assumption that the formation
151 of the tourmaline was coeval with, and has a genetic connection to, the host rocks.
152 Our work at Cuonadong shows that some tourmalines in the granite/pegmatite may be
153 inherited and thus unrelated to the host granite. Two lines of evidence support the
154 inherited origin of Tur P: 1) Monazite grains in the pegmatites and two-mica \pm

155 tourmaline granites yielded ages of ca. 20 Ma (Fig. 2b), whereas the Tur P $^{40}\text{Ar}/^{39}\text{Ar}$
156 dating yielded an Eocene age of ca. 40 Ma, coincided with the presence of two
157 Eocene monazite grains in the granite (Figs. 2a, b), and significantly older than the
158 crystallization age of the host pegmatites; 2) The common occurrence of fractures in
159 these tourmalines and the presence of the pegmatite mineral assemblages in the
160 fractures suggests that they predate the pegmatites (Figs. 1a-d).

161 Several lines of evidence suggest that the two-mica granite and pegmatite
162 evolved in a cogenetic system, with the pegmatite magmas representing the late
163 evolved phase: 1) They yield comparable ages; 2) Both the granite and pegmatite
164 have similar mineral assemblages consisting of plagioclase, k-feldspar, muscovite \pm
165 tourmaline; 3) The occurrences of the pegmatites as veins or pockets in the granites,
166 without clear boundaries between them (Supplementary Fig. 2); 4) Xie et al. (2020)
167 studied zircon grains in the granite and pegmatite at Cuonadong and proposed
168 magmatic evolution from the granites to pegmatites based on the Zr/Hf ratios of
169 zircon.

170 However, Tur P should be xenocrysts in the host granitoids. In a cogenetic
171 system, tourmaline crystallized in early-stage granite should have higher V contents
172 compared to those formed in a late pegmatite because V is preferentially fractionated
173 into early-crystallized ilmenite, biotite and tourmaline during magma crystallization
174 (van Hinsberg, 2011). Therefore, if Tur P is a primary phase in the host pegmatite, it
175 should have lower V contents than Tur G which represents the early crystallization
176 stage (two-mica granite). However, the obviously higher V concentrations in Tur P

177 suggest that it was not a product of the same Miocene magmatism as the host
178 pegmatite ([Supplementary Table 3](#)).

179 What was the source of the Eocene Tur P and how was it incorporated in the
180 Miocene leucogranite? Based on $^{40}\text{Ar}/^{39}\text{Ar}$ geochronology, the Tur P formed at ca. 40
181 Ma. These ages are coeval with the emplacement ages of the Yardoi granitoids ([Zeng
182 et al., 2011; Hou et al., 2012](#)), which is ca. 100 km north of Cuonadong and one of the
183 few occurrences of Eocene intrusions in the northern Tethyan Himalaya
184 ([Supplementary Fig. 1](#)). The Yardoi granitoids were interpreted to have formed from
185 the partial melting of the lower crust of the India plate during Eocene crustal
186 thickening and the subsequent Neo-Tethyan slab break-off in the early stage of the
187 India-Asian collision ([Fig. 3a; Zeng et al., 2011; Hou et al., 2012](#)). Tourmalines are
188 not common in the Yardoi granitoids but recent boron isotope analyses showed that
189 the $\delta^{11}\text{B}$ values of the Yardoi granitoids range from -8.9‰ to -6.6‰ ([Fig. 2c; Hu et al.,
190 2018](#)), partially overlapping with those of Tur P having ranges of -14.14‰ to -7.06‰
191 (average -9.76‰). However, $\delta^{11}\text{B}$ values for Tur P are relatively lighter,
192 approximating the average boron isotopes of continental crust ($-10 \pm 3\%$, [Marschall
193 and Jiang, 2011](#)), whereas the Yardoi and the Miocene tourmalines at Cuonadong (Tur
194 G) have higher $\delta^{11}\text{B}$ values. The differences may suggest more involvement of lower
195 crust (mafic magma) during crustal anatexis for the latter ([Fig. 2d](#)), supported by
196 regional tectonic evolution models for the Eocene Yardoi granitoids and Miocene
197 Cuonadong leucogranite ([Hou et al., 2012; Wu et al., 2020](#)). We propose that partial
198 melting of upper crustal materials may have occurred in the Cuonadong area during

199 Eocene crustal thickening, when shear heating elevated the surface heat flow (Hartz
200 and Podladchikov, 2008), causing the temperature to reach the solidus, generating the
201 felsic magmatism and forming Tur P (Figs. 3a). During later geologic events, the Tur
202 P was preserved due to their robustness (Marschall and Jiang, 2011; Slack and
203 Trumbull, 2011). The widespread Miocene leucogranite magmatism (including the
204 early-stage two-mica granite and late evolved pegmatite phase), formed either by
205 decompressional melting of the crust (Wu et al., 2020) or extensive long-living shear
206 heating (Whittington et al., 2009; Hou et al., 2012) linked to Indian plate rollback and
207 breakoff (DeCelles et al., 2011). The magma ascended to the upper crust (Fig. 3a)
208 where the late pegmatite phase in the upper part of the two-mica granite incorporated
209 the early-stage Eocene granitoids and Tur P at shallow levels in the crust (Figs. 3b, c).
210 Although no Eocene tourmaline has been found in the two-mica granite, the presence
211 of Eocene-age monazite xenocrysts (Fig. 2b) are consistent with assimilation of
212 Eocene granites by the Miocene granite at Cuonadong.

213 Our studies document the spatial coexistence of Miocene and Eocene
214 magmatism in the Tethyan Himalaya and suggest petrogenesis through upper crust
215 anatexis during shear heating for the Eocene magmas in Southern Tibet. The presence
216 of inherited tourmaline means that the K/Ar clock in the tourmaline was not reset by
217 thermal diffusion during the emplacement of the granitic pegmatite, perhaps due to
218 the high closure temperature and low diffusion rates for major and trace elements
219 within the tourmaline lattice (Dutrow and Henry, 2011). Thus, caution must be used
220 when applying tourmaline geochemistry to the investigation of the petrogenesis of the

221 host magmatic rocks.

222 **Acknowledgements**

223 This study was funded by the National Natural Science Foundation of China
224 (41725009), and the Fundamental and Applied Fundamental Research Major Program
225 of Guangdong Province (2019B030302013). We appreciate comments by Calvin
226 Barnes, Nadia Mohammadi and an anonymous reviewer on this paper.

227 **References**

- 228 DeCelles, P.G., Kapp, P., Quade, J., and Gehrels, G.E. (2011) Oligocene–Miocene Kailas basin,
229 southwestern Tibet: Record of postcollisional upper-plate extension in the Indus-Yarlung
230 suture zone. *Geological Society of America Bulletin*, 123, 1337–1362.
- 231 Dutrow, B.L., and Henry, D.J. (2011) Tourmaline: A Geologic DVD. *Elements*, 7, 301–306.
- 232 Harrison, T.M., Mckeegan, K.D. and LeFort, P. (1995) Detection of inherited monazite in the
233 Manaslu leucogranite by $^{208}\text{Pb}/^{232}\text{Th}$ ion microprobe dating. *Chemical Geology*, 133,
234 271–282.
- 235 Hartz, E.H., and Podladchikov, Y.Y. (2008) Toasting the jelly sandwich: The effect of shear
236 heating on lithospheric geotherms and strength. *Geology*, 36, 331–334.
- 237 Hou, Z.Q., Zheng, Y.C., Zeng, L.S., Gao, L.E., Huang, K.X., Li, W., Li, Q.Y., Fu, Q., Liang,
238 W., and Sun, Q.Z. (2012) Eocene–Oligocene granitoids in southern Tibet: Constraints on
239 crustal anatexis and tectonic evolution of the Himalayan orogen. *Earth and Planetary
240 Science Letters*, 349–350, 38–52.
- 241 Hu, G.Y., Zeng, L.S., Gao, L.E., Liu, Q.P., Chen, H., and Guo, Y.S. (2018) Diverse magma
242 sources for the Himalayan leucogranites: Evidence from B-Sr-Nd isotopes. *Lithos*,
243 314–315, 88–99.
- 244 Kelley, S. (2002) Excess argon in K–Ar and Ar–Ar geochronology. *Chemical Geology*, 188,
245 1–22.
- 246 Launay, G., Sizaret, S., Guillou-Frottier, L., Gloaguen, E., and Pinto, F. (2018) Deciphering
247 fluid flow at the magmatic-hydrothermal transition: A case study from the world-class
248 Panasqueira W–Sn–(Cu) ore deposit (Portugal). *Earth and Planetary Science Letters*, 499,
249 1–12.
- 250 Lee, J.Y., Marti, K., Severinghaus, J.P., Kawamura, K., Yoo, H.S., Lee, J.B., and Kim, J.S.
251 (2006) A redetermination of the isotopic abundances of atmospheric Ar. *Geochimica et
252 Cosmochimica Acta*, 70, 4507–4512.
- 253 Li, G.M., Zhang, L.K., Jiao, Y.J., Xia, X.B., Dong, S.L., Fu, J.G., Liang, W., Zhang, Z., Wu,
254 J.Y., Dong, L., and Huang, Y. (2017) First discovery and implications of Cuonadong
255 superlarge Be-W-Sn polymetallic deposit in Himalayan metallogenic belt, southern Tibet.
256 *Mineral Deposits*, 36, 1003–1008 (in Chinese with English abstract).
- 257 Marschall, H.R., and Jiang, S.Y. (2011) Tourmaline Isotopes: No Element Left Behind.
258 *Elements*, 7, 313–319.
- 259 Patiño Douce, A.E., and Harris, N. (1998) Experimental constraints on Himalayan anatexis.
260 *Journal of Petrology*, 39, 689–710.

- 261 Qiu, H.N., Pu, Z.P. and Dai, T.M. (2007) Occurrences of Excess ^{40}Ar in Hydrothermal
262 Tourmaline: Interpretations from ^{40}Ar - ^{39}Ar Dating Results by Stepwise Heating. *Acta*
263 *Geologica Sinica*, 81, 51–516.
- 264 Schärer, U. (1984) The effect of initial ^{230}Th disequilibrium on young U/Pb ages: the Makalu
265 case, Himalaya. *Earth and Planetary Science Letters*, 67, 191–204.
- 266 Slack, J.F., and Trumbull, R.B. (2011) Tourmaline as a Recorder of Ore-Forming Processes.
267 *Elements*, 7, 321–326.
- 268 Thern, E.R., Blereau, E., Jourdan, F., and Nelson, D.R. (2020) Tourmaline $^{40}\text{Ar}/^{39}\text{Ar}$
269 geochronology and thermochronology: Example from the youngest
270 Hadean-zircon-bearing siliciclastic metasedimentary rocks from the Yilgarn Craton.
271 *Geochimica et Cosmochimica Acta*, 277, 285–299.
- 272 van Hinsberg, V.J. (2011) Preliminary experimental data on trace element partitioning
273 between tourmaline and silicate melt. *Canadian Mineralogist*, 49, 153–163.
- 274 van Hinsberg, V. J., Henry, D.J., and Dutrow, B.L. (2011) Tourmaline as a Petrologic Forensic
275 Mineral: A Unique Recorder of Its Geologic Past. *Elements*, 7, 327–332.
- 276 Whittington, A.G., Hofmeister, A.M. and Nabelek, P.I. (2009) Temperature-independent
277 thermal diffusivity of the Earth's crust and implication for magmatism. *Nature*, 458,
278 319–321.
- 279 Wu, F.Y., Liu, Z.C., Liu, X.C. and Ji, W.Q. (2015) Himalayan leucogranite: Petrogenesis and
280 implications to orogenesis and plateau uplift. *Acta Petrologica Sinica*, 31, 1–36 (in
281 Chinese with English abstract).
- 282 Wu, F.Y., Liu, X.C., Liu, Z.C., Wang, R.C., Xie, L., Wang, J.M., Ji, W.Q., Yang, L., Liu, C.,
283 Khanal, G.P., and He, S.X. (2020) Highly fractionated Himalayan leucogranites and
284 associated rare-metal mineralization. *Lithos*, 352-353, doi: 10.1016/j.lithos.2019.105319.
- 285 Xie, L., Tao, X., Wang, R., Wu, F., Liu, C., Liu, X., Li, X., and Zhang, R. (2020) Highly
286 fractionated leucogranites in the eastern Himalayan Cuonadong dome and related
287 magmatic Be–Nb–Ta and hydrothermal Be–W–Sn mineralization. *Lithos*, 354-355, doi:
288 10.1016/j.lithos.2019.105286.
- 289 Yang, S.Y., Jiang, S.Y., and Palmer, M.R. (2015) Chemical and boron isotopic compositions
290 of tourmaline from the Nyalam leucogranites, South Tibetan Himalaya: Implication for
291 their formation from B-rich melt to hydrothermal fluids. *Chemical Geology*, 419,
292 102–113.
- 293 Yin, A. (2006) Cenozoic tectonic evolution of the Himalayan orogen as constrained by
294 along-strike variation of structural geometry, exhumation history, and foreland
295 sedimentation. *Earth-Science Reviews*, 76, 1–131.
- 296 Yin, A., and Harrison, T.M. (2000) Geologic evolution of the Himalayan-Tibetan orogen.
297 *Annual review of earth and planetary sciences*, 28, 211–280.
- 298 Zeng, L.S., Gao, L.E., Xie, K.J., and Liu-Zeng, J. (2011) Mid-Eocene high Sr/Y granites in
299 the Northern Himalayan Gneiss Domes: Melting thickened lower continental crust. *Earth*
300 *and Planetary Science Letters*, 303, 251–266.
- 301 Zhou, Q., Li, W., Wang, G., Liu, Z., Lai, Y., Huang, J., Yan, G., and Zhang, Q. (2019)
302 Chemical and boron isotopic composition of tourmaline from the Cuonadong
303 leucogranite-pegmatite system in South Tibet. *Lithos*, 326-327, 529–539.

304 **Figure captions**

305 **Fig. 1** (a) Hand specimen of the Cuonadong pegmatites, showing abundant fractures
306 in the tourmaline grains. A part of a thin section was scanned as insert, showing the
307 common occurrences of fractures in Tur P; (b) Another sample of the Cuonadong
308 pegmatites showing fractured tourmaline; (c) Photomicrograph showing Tur P
309 crosscut by a quartz vein in pegmatite; (d) Photomicrograph showing Tur P crosscut
310 by a quartz-muscovite vein in pegmatite; (e) The crystal habit of tourmaline (Tur G)
311 in the two-mica ± tourmaline granite.

312 **Fig. 2** (a) Plateau $^{40}\text{Ar}/^{39}\text{Ar}$ dating results, and $^{36}\text{Ar}/^{40}\text{Ar}$ versus $^{39}\text{Ar}/^{40}\text{Ar}$ normal and
313 inverse isochron plots of the Tur P; (b) and (c) Monazite geochronological results of
314 the Cuonadong leucogranites; (d) Boron isotope compositions of the Tur P and Tur G
315 and comparison with various boron reservoirs in nature (after Marschall and Jiang,
316 2011; Hu et al., 2018).

317 **Fig. 3** (a) Schematic regional section showing the Eocene Yardoï granitoids and
318 granitoids at Cuonadong (100 km south to Yardoï) during crustal thickening. The
319 large-scale Miocene Himalayan leucogranites due to intense activity of the STD and
320 HHS extrusion emplaced at Cuonadong area. STD: South Tibetan Detachment; MCT
321 = Main Central Thrust; MBT: Main Boundary Thrust; HHS = High Himalayan
322 Sequence; THS = Tethyan Himalayan Sequence; IYS = Indus-Yarlung suture; GTS =
323 Gangdese thrust system; (b) A simplified cartoon for emplacement of the Miocene
324 Cuonadong leucogranites, represented by the two-mica granite and the late cogenetic
325 pegmatite phase, and xenoliths of the Eocene granitic units containing Tur P; (c)
326 Schematic diagram showing the capture of the Eocene Tur P by the Miocene

- 327 pegmatites at Cuonadong. Pl = plagioclase; Qz = quartz; Kfs = K-feldspar; Mnz =
328 monazite; Ms = muscovite.

Figure 1

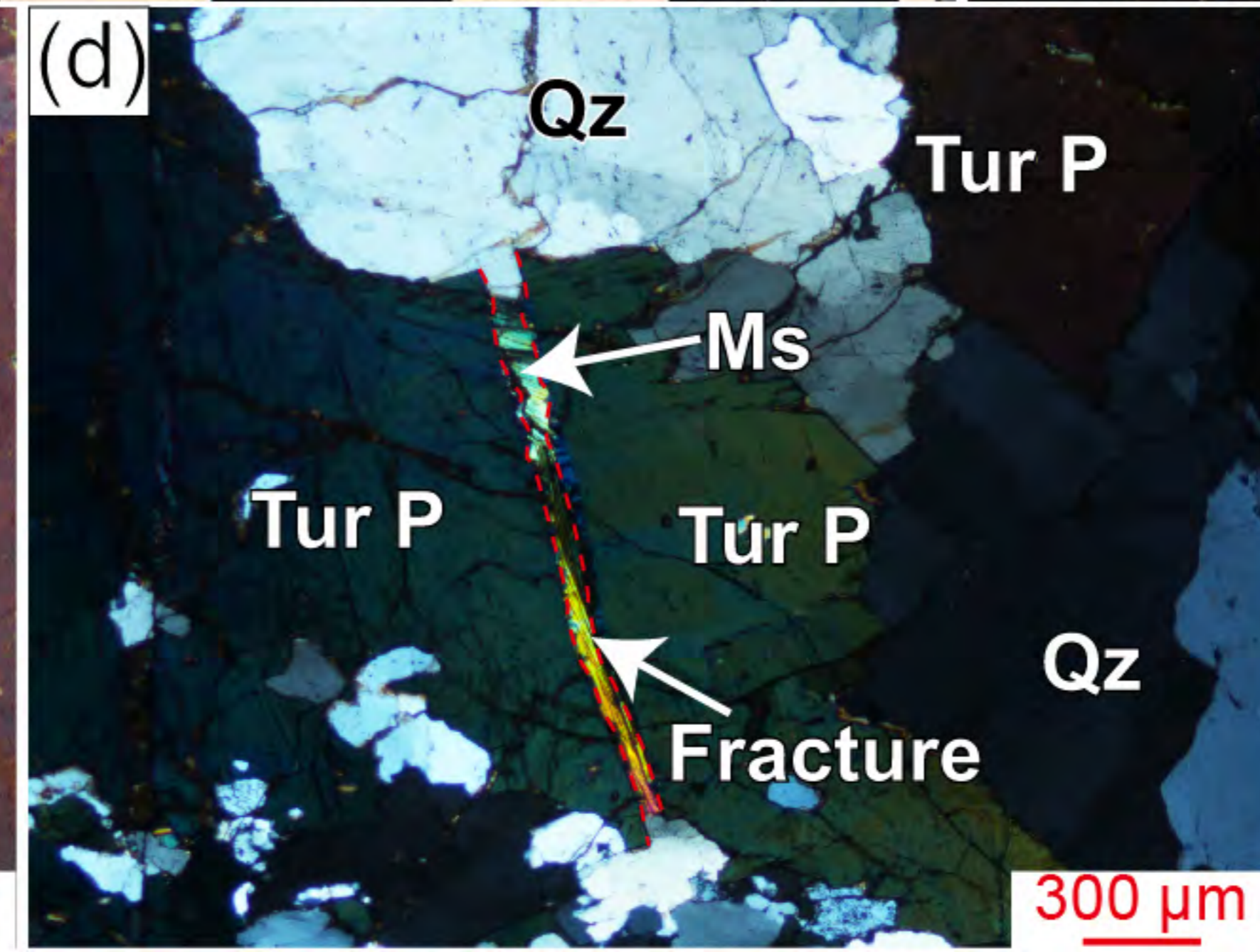
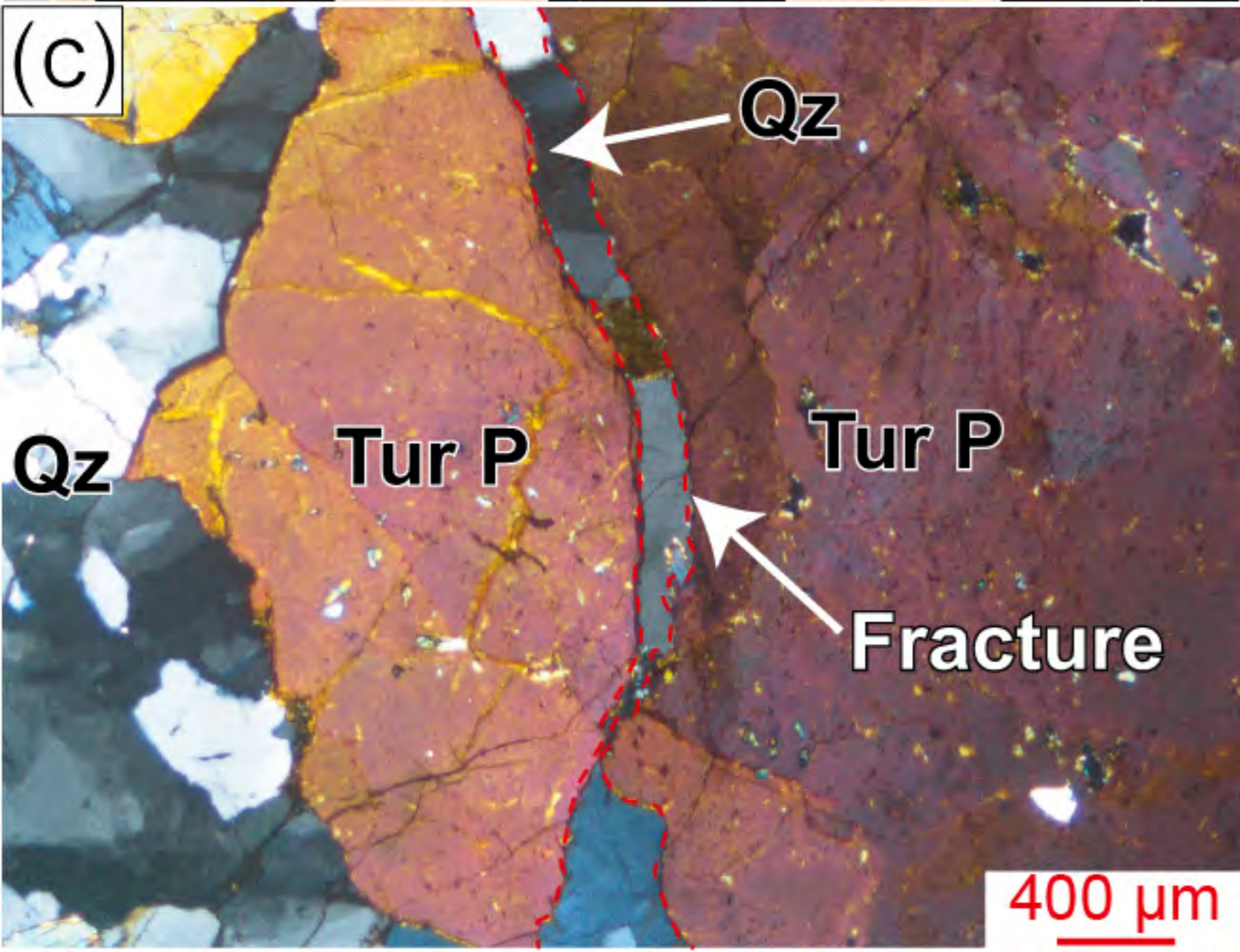
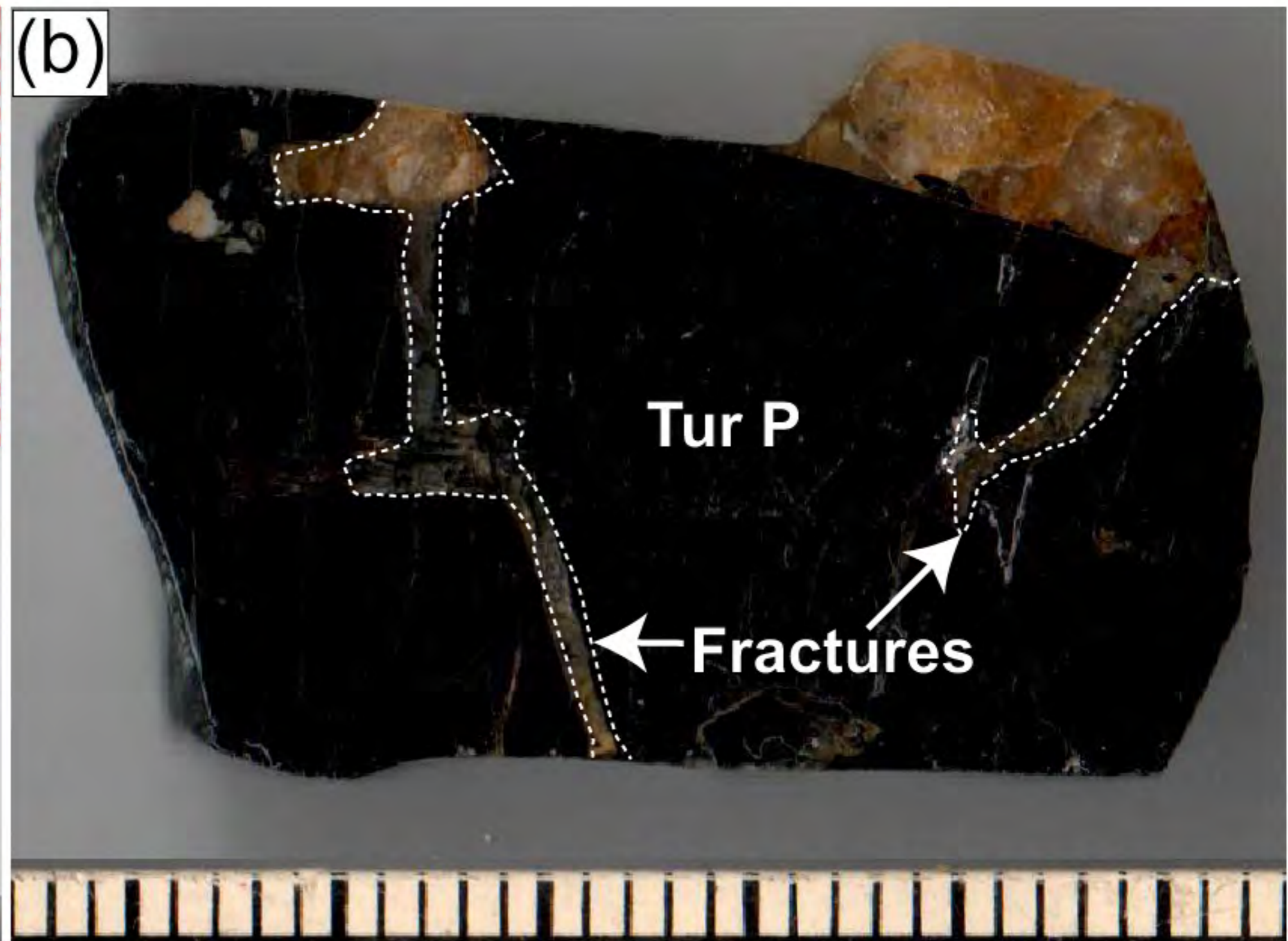
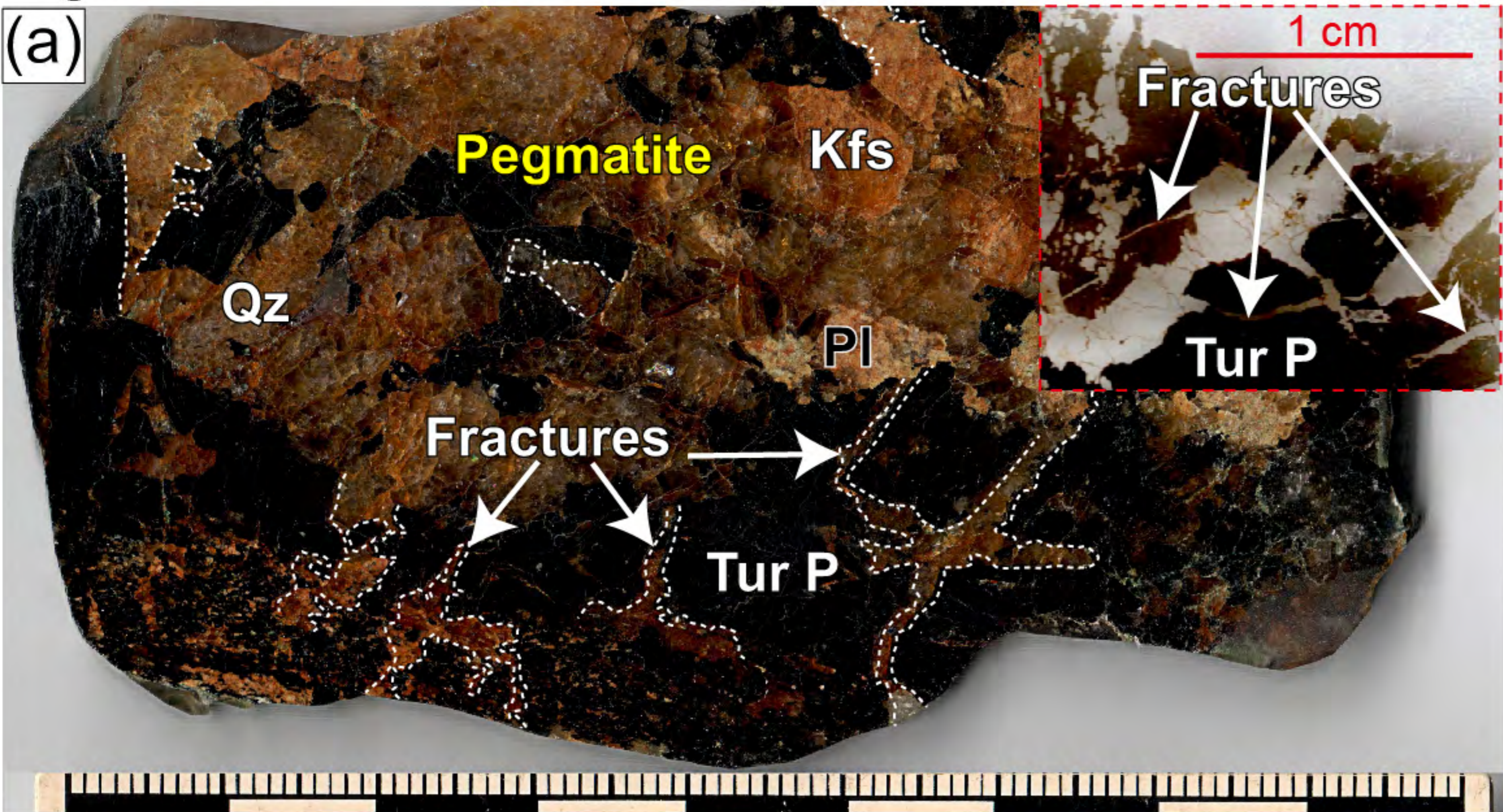


Figure 2

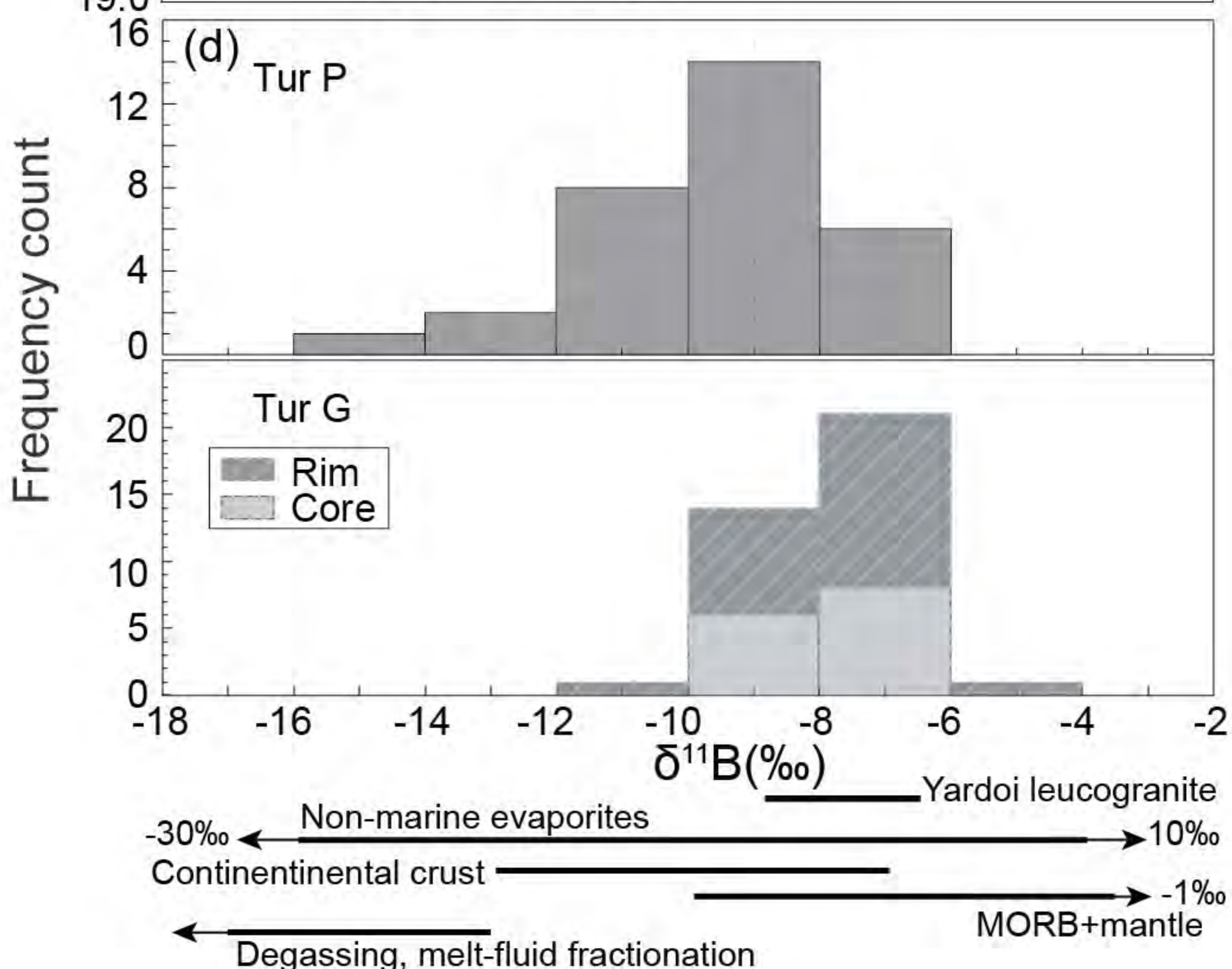
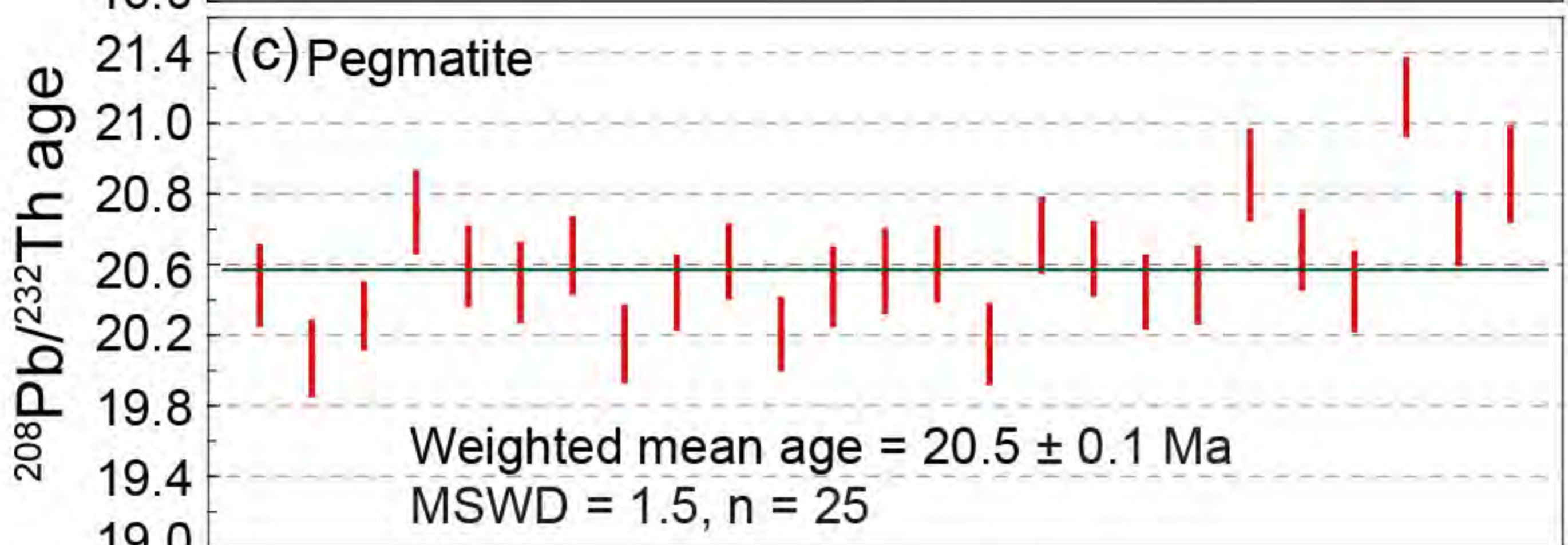
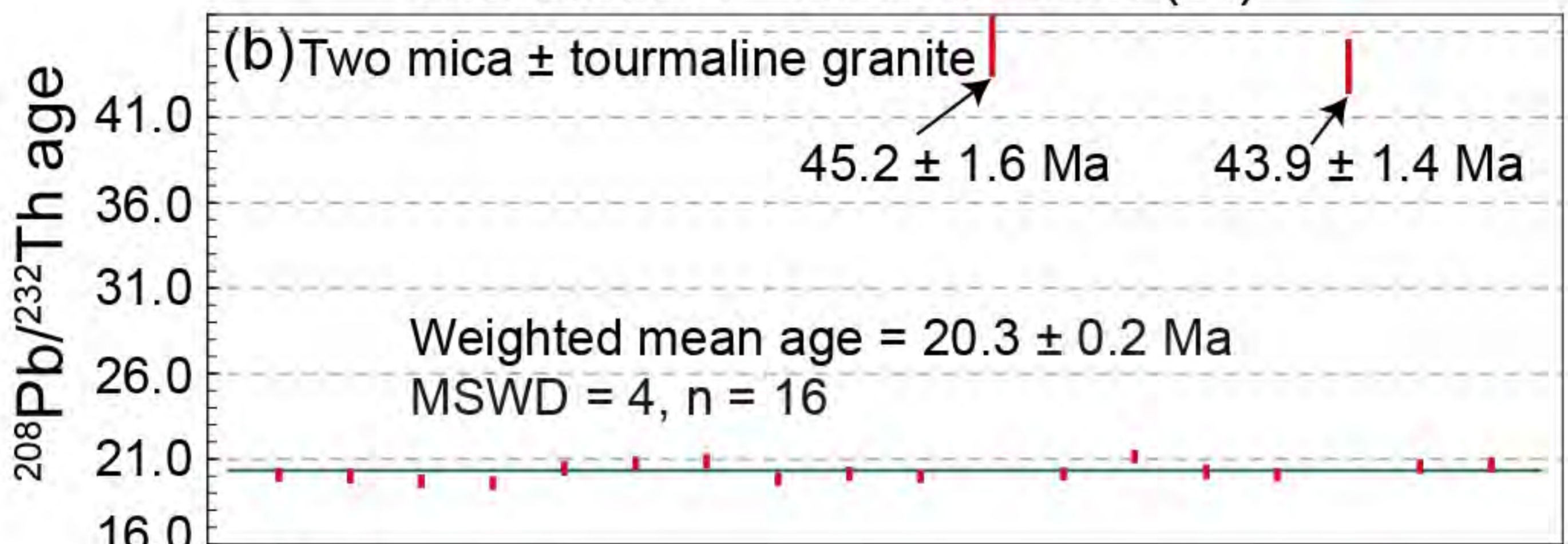
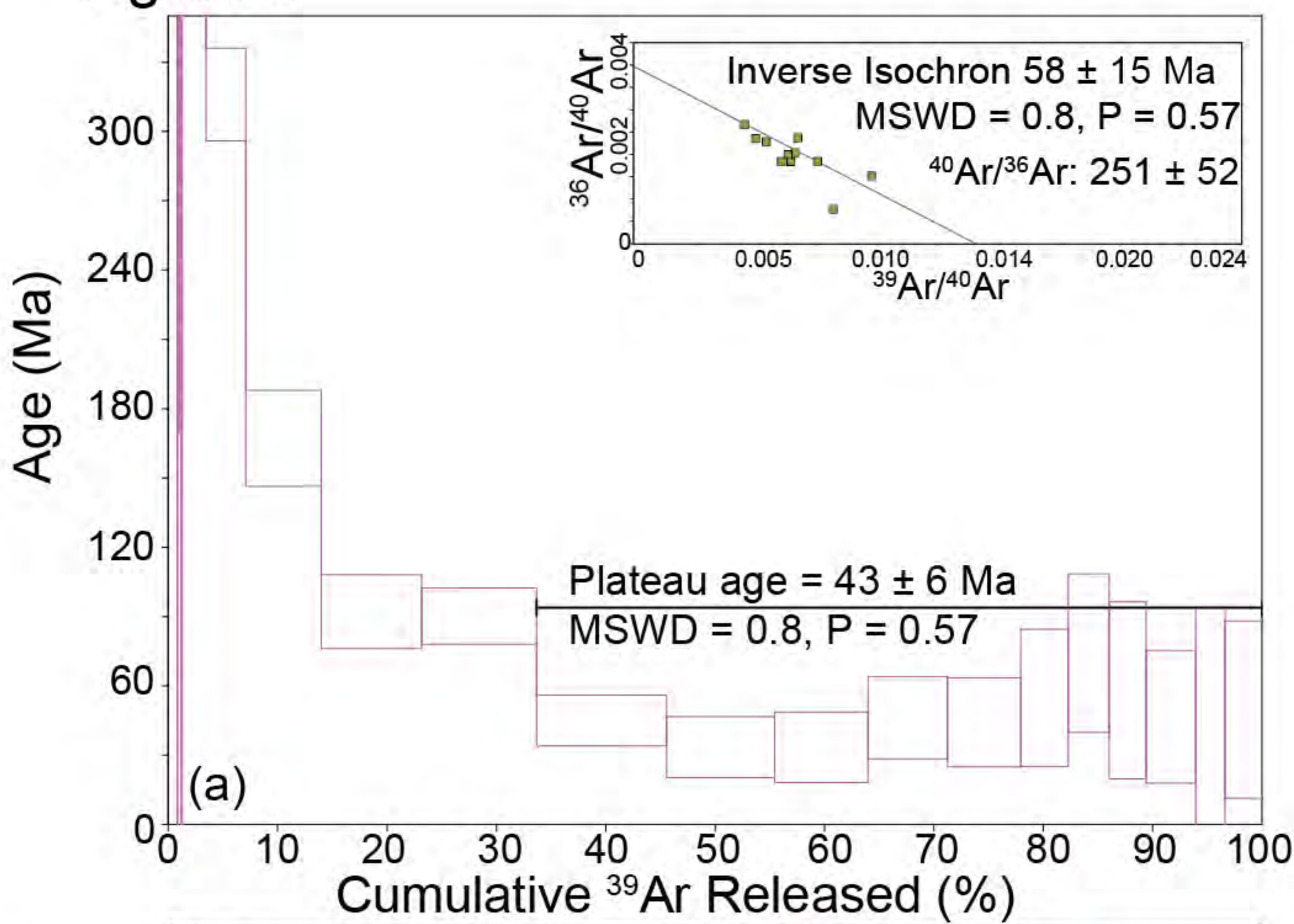


Figure 3

